# Selective Wireless Power Transfer Using Magnetic Field Editing

Xiaoyang Tian, *Student Member, IEEE*, Kwok T. Chau, *Fellow, IEEE*, Wei Liu, *Student Member, IEEE*, and Christopher H. T. Lee, *Senior Member, IEEE*

***Abstract*—This article proposes and implements a selective wireless power transfer (WPT) system based on magnetic field editing technology. Compared with the traditional WPT without control of power regions, the proposed system can deliver the energy with higher safety, flexibility, selectivity, and can be applied to multiple receivers. The algorithms for current calculation and synchronized control strategies are given to construct the desired magnetic field effectively. The optimization process based on the receiver configuration and voltage threshold is also demonstrated. Both simulation and experimental results validate that the magnetic field distribution can be arbitrarily edited through the proposed current control strategy, and realize the selectivity of the powering area. A prototype of the proposed system with five transmitters is constructed and tested, which can successfully deliver wireless power of 14 W over the distance of three times larger than the radius of the receiver coil with the transmission efficiency over 79%.**

***Index Terms*—Magnetic field editing (MFE), multiple receivers, multiple transmitters, selectivity, wireless power transfer (WPT).**

## I. Introduction

THE energy and information security problems have always been a vital issue in many commercial and industrial applications [1]–[3]. As the wireless power transfer (WPT) technology is more and more widely adopted to take place of the traditional cabled power transmission [4]–[6], there are raising concerns on its security and controllability [7], [8]. For instance, the roadway-powered electric vehicles (EV) system proposed in [9] successfully breaks the limitation of the fixed charger. But for a road with multiple users, the protection of power transmission paths remains to be a tricky problem. On fundamental bases, the WPT systems share many similar principles in common with the communication systems [10]–[12]. Thus, it is natural to raise equal concerns to WPT security as to wireless communication and information security.

Manuscript received May 12, 2020; revised July 6, 2020; accepted August 5, 2020. Date of publication August 17, 2020; date of current version October 30, 2020. This work was supported by the Hong Kong Research Grants Council, Hong Kong Special Administrative Region, China, under Project 17207420. Recommended for publication by Associate Editor O. C. Onar. *(Corresponding author: K. T. Chau.)*

Xiaoyang Tian, Kwok T. Chau, and Wei Liu are with the Department of Electrical and Electronic Engineering, The University of Hong Kong, Hong Kong, China (e-mail: xytian@eee.hku.hk; ktchau@eee.hku.hk; liuwei@eee.hku.hk).

Christopher H. T. Lee is with the School of Electrical and Electronic Engineering, Nanyang Technological University, Singapore 639798, Singapore (e-mail: chtlee@ntu.edu.sg).

Color versions of one or more of the figures in this article are available online at https://ieeexplore.ieee.org.

Digital Object Identifier 10.1109/TPEL.2020.3017000

For cabled power transmission systems or local chargers with batteries, each user has only one port for the plug-in. Therefore, it is easy to set up a communication system to realize the identification process. While in WPT systems, the power is exposed to the whole area and easy to be leaked and stolen. To solve this problem, a wireless power encryption system based on chaotically regulating the switching frequency is proposed in [13]. An adjustable compensation capacitor matrix is adopted in the system to match the time-varying frequency, so that only the authorized receiver can always be in resonance with the transmitter. The encryption system is further improved in [14] by regulating the frequency as well as the duration to generate a two-dimensional password. The encryption performance is impressive provided that a wide frequency range is allowable. However, for some applications, the usable frequency band may be very limited. For instance, the general operating frequency for wireless charging of EVs usually ranges within 80–120 kHz. Under this situation, unauthorized users could steal some wireless energy.

Recently, a new technology called magnetic multiple-input multiple-output (MIMO) was proposed in [11]. The load current is maximized by controlling the transmitter currents based on mutual inductances. The beamformed magnetic flux density can be maximized at the targeted point. An adaptive phased array control of transmitter currents is adopted in [15] and [16] to realize the magnetic beamforming. The leakage field can be effectively controlled. However, overall system efficiency is still less than 50% [15].

Another newly developed control method, which is called the synthesized magnetic field (SMF) focusing technology, is proposed in [17] and has been successfully implemented for some applications [18]. The proposed system can reform the magnetic field distribution through the current control, hence realizing the desired magnetic flux density at a particular position. However, relevant research is focused on synthesizing the magnetic field at a single point or in a small area. Besides, the adjustable inductance array used for phase control will inevitably reduce the system efficiency, and how to delicately control and efficiently edit the magnetic flux density for specific WPT systems is still uncertain. Also, the dynamic characteristics of the WPT systems using this technology are unexplored.

Based on these crucial improvable aspects and the ingenuity of the SMF technology, the purpose of this article is to propose a new WPT system with more selectivity and controllability based on magnetic field editing (MFE) technology. The basic

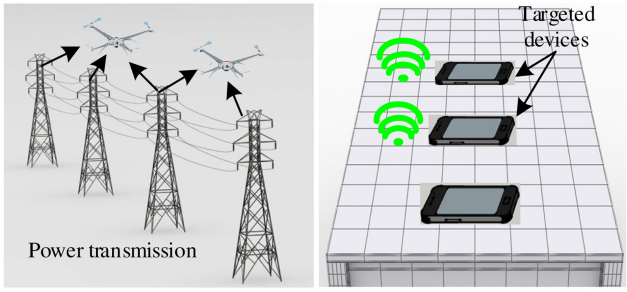


Fig. 1. Applications of MFE technology. (a) Targeted dynamic charging for drones. (b) Selective wireless charging for phones.

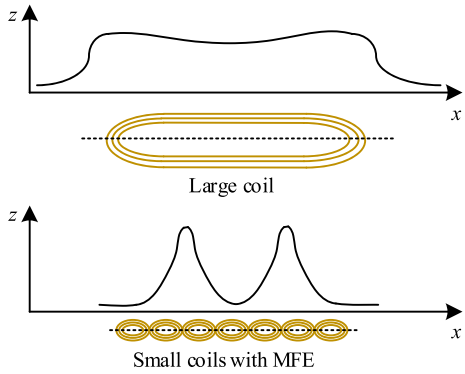


Fig. 2. Comparison of magnetic flux density distributions.

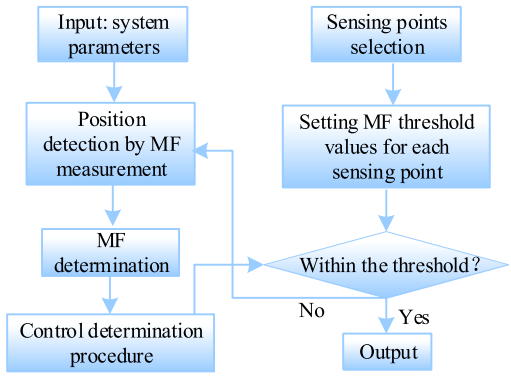


Fig. 3. Flow chart of the proposed system logic.

principle is to control the upper and lower threshold of the functional component of the magnetic flux density at different regions of the coverage area, hence only the targeted regions can get access to the usable energy. Compared with traditional systems, the proposed one takes the definite advantage that the magnetic flux density is generated by predetermined currents and the corresponding control. Thus, overall system efficiency can be flexibly optimized for different application scenarios. Meanwhile, the complicated high-frequency phase-locking is avoided [16], [19], thus the system efficiency can be further improved.

The rest of this article is organized as follows. Section II will describe the system configuration. Then, the principle of the proposed MFE will be described in Section III. Section IV will present the circuit analysis, current optimization, and control strategy. In Section V, system prototyping and experimental verification will be given. Finally, the conclusion will be drawn in Section VI.

## II. System Configuration

Via the design of system configuration as well as the control strategy, the proposed system can be embedded into many different scenarios, such as the targeted dynamic charging and selective wireless charging as shown in Fig. 1.

The basic principle of the so-called MFE technology is using specific algorithms to adjust and integrate the resonant currents in the transmitter system to generate the magnetic field, which can be either dynamic or static, and to infinitely approximate the desired one, as shown in Fig. 2.

There exist two tradeoffs: one lies between maximizing the magnetic field on intended positions and minimizing the intensity on unintended positions; another is between the system complexity and the degree of freedom in control. Thus, it is necessary to choose the appropriate system parameters for different applications, such as the transmission distance, the power level, the rightful frequency, and the acceptable threshold value of the electrical parameters. After identifying the position of the receivers, the control system can adjust the control variables to guarantee optimum currents flowing in the transmitter coils accordingly. Then, the validation should be made to make sure that under the predetermined controlling signal, the formed magnetic field (MF) is within the desired ranges at every concerning point and the practical requirements can be satisfied. The flow chart of the proposed system logic is shown in Fig. 3.

The system contains two-step control procedures. First, based on the system requirements and the position detection results of the receivers, the optimum value of the magnetic field density at each intended position should be calculated, and the accordant current values should also be determined. Then, the control signals will be further optimized and sent to the converters to achieve high system efficiency and good overall performance. In a word, with the proper control strategies, the induced magnetic field can be arbitrarily edited based on requirements. Thus, the energy can be directly transmitted to the charging target(s) with less magnetic flux leakage compared with the traditional multicoil WPT system [20]. Under the condition of the same input power, the proposed selective WPT system can further raise the security performance as well as the transmission efficiency.

## III. Magnetic Field Editing Technology

The proposed transmission system is shown in Fig. 4, where the intended position is located at an arbitrary point $(x_p, d)$. Generally, the intended positions can be extended to more than one point. Consequently, the corresponding magnetic field energy $\mathbf{B}$ can be attained by varying the currents in the transmitter array using the proposed control strategy. The merit of the system is that all the control can be conducted on the primary side.

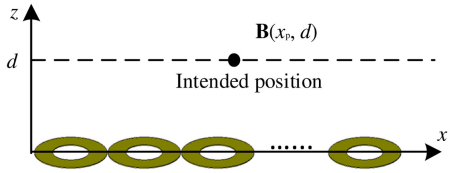


Fig. 4. Transmitter array.

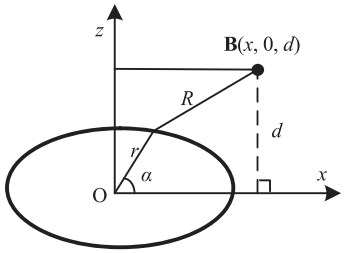


Fig. 5. Magnetic flux density generated by a circular filament.

The total magnetic flux density at the intended position can be calculated as the sum of all magnetic fields generated by the currents flowing in the transmitter array as given by

$$\mathbf{B} = \sum_{i=0}^{n} \mathbf{B}_i \tag{1}$$

where $n$ denotes the number of controllable currents. As shown in Fig. 5, each transmitter coil can be modelled as a set of circular filaments with different radii and carrying the same current. Thus, it is necessary to analyze and obtain a relatively simple and doable equation of the magnetic flux density generated by a single circular filament at an arbitrary position in three dimensions.

Under the configuration shown in Fig. 5, the magnetic flux density at the targeted point generated by a single coil can be expressed as [18]

$$d\vec{B} = \frac{\mu_0 I r d\alpha}{4\pi R^2}\vec{e}_\alpha \times \vec{e}_R = \frac{\mu_0 I r d\alpha}{4\pi R^2}\left(\frac{d}{R}\vec{e}_r + \frac{r-x}{R}\vec{e}_z\right) \tag{2}$$

and $R$ is given by

$$R^2 = (r\cos\alpha - x)^2 + (r\sin\alpha)^2 + d^2 \tag{3}$$

where $\vec{e}_\alpha$ and $\vec{e}_r$ denote the tangential and radial direction of the coil, respectively, $\vec{e}_R$ denotes the direction vector pointing from the finite current element to the targeted point, and $x$ and $d$ denote the horizontal and vertical coordinates of the targeted point, respectively. Thus, the magnetic density along the $z$-axis direction can be expressed as

$$\vec{B}_z = \int_0^{2\pi} \frac{\mu_0 I r(r-x)\vec{e}_z}{4\pi R^3} d\alpha. \tag{4}$$

It can be found in (4) that when $x < r$, the projection of the sensing point is inside the range of transmitter coil, and the direction of magnetic density at the targeted point is along the $z$-axis. While for $x > r$, the direction is reversed. For $x = r$, the magnetic density does not have a $z$-axis component. In the proposed system, the sensing point is relatively smaller than the transmitter. Thus, it is the outside range case that matters. To further analyze this scenario, there are two assumptions

$$\begin{cases} x = nr \\ d = ar \end{cases} \tag{5}$$

where $n$ and $a$ denote the ratio between the horizontal and vertical coordinates to the radius of the circular filament, respectively. By using (3) and (5), (4) can be further derived as

$$\vec{B}_z = \int_0^{2\pi} \frac{\mu_0 I r(r-x)\vec{e}_z}{4\pi R^3} d\alpha = AI \cdot \vec{e}_z \tag{6}$$

where $A$ is given by

$$A = \frac{\mu_0}{4\pi r}\int_0^{2\pi} \frac{(1-n)}{(1+n^2+a^2-2n\cos\alpha)^{3/2}} d\alpha. \tag{7}$$

Equations (6) and (7) show that in the WPT system, the functional part of the flux density at concerning points can be only determined by the ratio between the relative positions and the coil radius, but not their absolute values. For a given system configuration, $A$ can be determined as a constant parameter. Fig. 6 shows the general variation of $A$ versus different position relationships between the concerning points and the given transmitter filament.

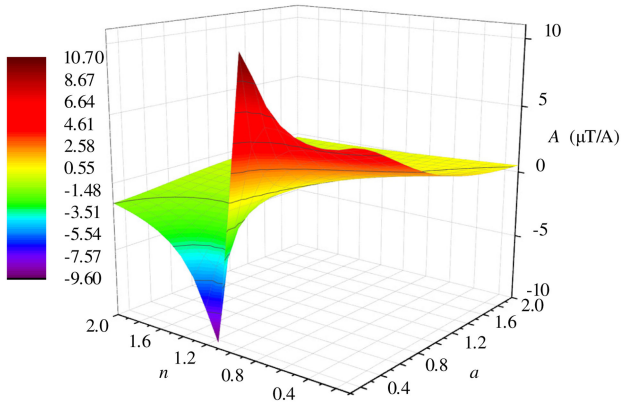


Fig. 6. Variation of $A$ of circular filament under different position relationships between transmitter and receiver.

It can be seen from Fig. 6 that the sign of $A$ is opposite when the targeted point is inside or outside of the circular filament while the absolute value decreases with the point moving away from the central point.

For generalization, when there are $p$ current sources and $q$ sensing points, the system relationship can be obtained as

$$\begin{bmatrix} \vec{B}_1 \\ \vec{B}_2 \\ \vdots \\ \vec{B}_q \end{bmatrix} = \begin{bmatrix} A_{11} & A_{12} & \cdots & A_{1p} \\ A_{21} & A_{22} & \cdots & A_{2n} \\ \vdots & \vdots & & \vdots \\ A_{q1} & A_{q2} & \cdots & A_{qp} \end{bmatrix} \begin{bmatrix} I_1 \\ I_2 \\ \vdots \\ I_p \end{bmatrix}. \tag{8}$$

All elements of the $A$-matrix in (8) are calculable and the desired magnetic densities can be achieved through the optimal control of the currents in different transmitter coils. Theoretically, under the severest condition, if the magnetic field at every

sensing point is all required to be fixed constants, the system can only allow the number of sensing points to be as much as the number of the transmitter coils. Otherwise (8) will become unsolvable. Thus, the more the transmitter coils are adopted in the system, the more sensing points can be allowed and the higher the accuracy of the editing procedure will achieve. While in practice, for example in the wireless charging systems, because of the mechanism based on the threshold charging voltage, the charging procedure will not be started as long as the output voltage does not reach the threshold. Thus, the conditions can be relaxed, which can allow more controllable points in the desired editing region to raise accuracy. Based on the analyzes before, the problem can be modelled as

$$\max \left|\vec{B}_a\right| (a \in [1, q]) \tag{9a}$$

$$\text{s.t. } \left|\vec{B}_u\right| \leq B_t (u = 1, 2 \ldots q, u \neq a) \tag{9b}$$

where $B_a$ and $B_u$ denote magnetic flux density at the authorized or unauthorized positions, respectively, while $B_t$ denotes the predetermined threshold value. Combined with (8), the model (9) can be solved with a particular set of transmitter current ranges, denoted by **S**, which can be considered as the minimum requirements of the transmitter currents to make sure the system works. It is worth mentioning that **S** is a range set that can be obtained in advance only through the predetermined threshold values of the magnetic field. The position information of the receiver is not necessarily needed in this calculation procedure which provides convenience in further current optimization. Normally, the total number of active users will be less than the number of transmitter currents so that the degree of freedom of the system is relatively high. Thus, there will be some room for the system to be further optimized. The model described by (9) therefore can be added with one or multiple objective functions, such as maximizing or minimizing the magnetic flux density at some specific sensing points, size of the receiver, or other practical requirements of the system. It should be noted when the position points are more than the number of controllable currents, the system is low degree of freedom so that (8) can become an overdetermined system. Under this situation, the least-square method [21] can be adapted to obtain an approximate solution. But still, (9) should be strictly satisfied with priority, or the selective performance may fail.

For the coil sizes shown in Fig. 7, the theoretical value of magnetic flux density on the $z$-axis before and after editing are compared and presented in Fig. 8. The transmitter array consists of 10 coils with the same sizes and to realize the magnetic field editing on a line of 1-m length. The sensing points are selected on the center of each transmitting coil, at the height of 150 mm. For comparison, a large coil with the same length and turns is designed and shown in Fig. 7(b). The system parameters are depicted in Table I. Based on the aforementioned algorithm, one of the possible sets of transmitter currents for three different editing scenarios are calculated and listed in Table II.

The unedited magnetic field distribution on the 1-m line generated by the large coil is shown in Fig. 8(a) while the editing results of targeting the magnetic field to both the 3rd and 8th coil

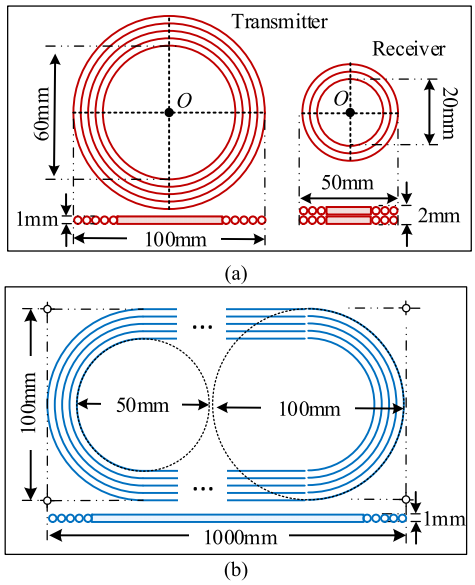


Fig. 7. Coil sizes. (a) Transmitter and receiver coil. (b) Large coil for comparison.

TABLE I
SYSTEM CONFIGURATION

| Items | Symbol | Value |
|---|---|---|
| Number of transmitter coils | $p$ | 10 |
| Number of sampling points | $q$ | 10 |
| Turns of each transmitter coil | $N_t$ | 20 |
| Turns of the receiver coil | $N_r$ | 30 |
| Turns of the comparison coil | $N_c$ | 20 |
| Hight of sensing line | $d$ | 150 mm |
| Frequency | $f$ | 1 MHz |

TABLE II
CURRENT VALUES AFTER EDITING

| Number | Current values for Fig. 8 (b) (A) | Current values for Fig. 8 (c) (A) | Current values for Fig. 8 (d) (A) |
|---|---|---|---|
| 1 | 0.1284 | 0.0041 | 0.0200 |
| 2 | -0.4345 | 0.0050 | -0.0345 |
| 3 | 1.2250 | 0.0021 | 0.1898 |
| 4 | -0.4268 | 0.0192 | -0.6232 |
| 5 | 0.1102 | -0.0340 | 1.7310 |
| 6 | 0.1102 | 0.1898 | -0.6231 |
| 7 | -0.4268 | -0.6228 | 0.1897 |
| 8 | 1.2250 | 1.7303 | -0.0340 |
| 9 | -0.4345 | -0.6192 | 0.0185 |
| 10 | 0.1284 | 0.1775 | 0.0040 |

can be shown in Fig. 8(b). The cases of targeting the magnetic field to a single point are shown in Fig. 8(c) and (d). All four cases are conducted under the condition of the same input power. It can be seen from the three different editing results that the magnetic flux densities at the targeted or authorized regions can be significantly improved by the magnetic field editing, and are much higher than that of the untargeted or unauthorized region. The flux density of the targeting points in Fig. 8(b) is about 1.5 times the original value, while that in Fig. 8(c) and (d) is about 2 times the original value.

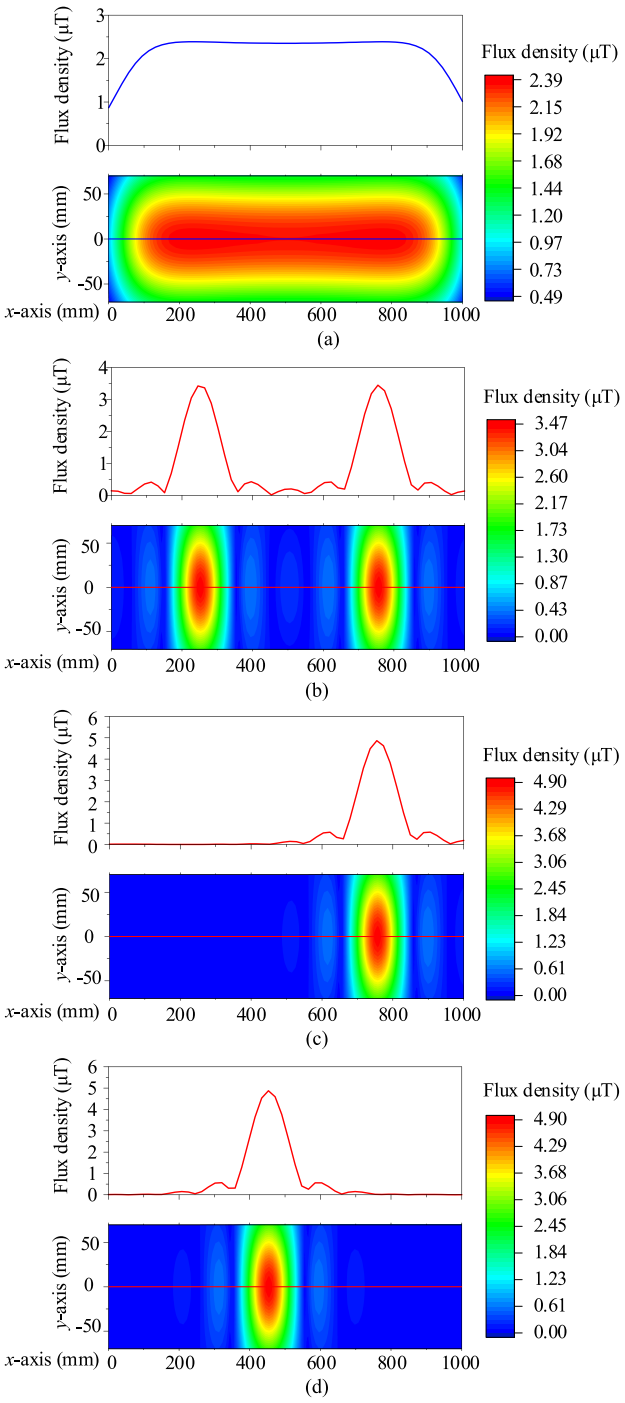


Fig. 8. Comparison of magnetic flux densities before and after editing. (a) Unedited magnetic field. (b) Target on both the 3rd and the 8th coils. (c) Target on the 8th coil. (d) Target on the 5th coil.

## IV. Current Optimization and Control Strategy

The main purpose of the proposed system is to generate a high-frequency-resonating magnetic field at the targeted points while suppressing the magnetic field at other positions to satisfy the requirement of selective WPT. With the presence of one or multiple receiver coils, the reflected impedance may occur differently to the transmitter coils.

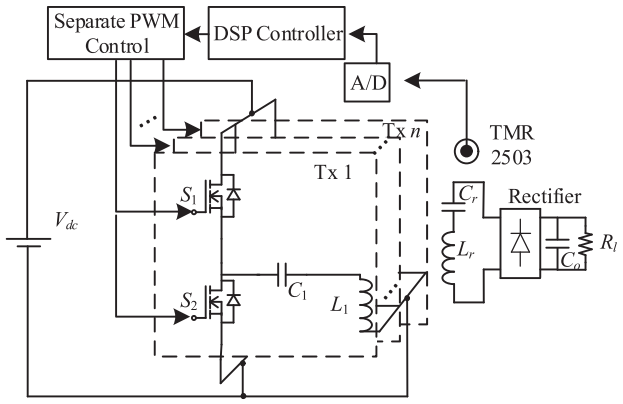


Fig. 9. System topology.

### A. Design Schemes

To achieve high system efficiency, the transmitter currents should be further optimized within the range obtained from (9). An appropriate control strategy should be determined accordingly. To flexibly control the currents in different transmitter (Tx) coils and reduce the system complexity, the half-bridge inverters are used to generate the desired control voltages. For the system with *n* Tx coils, the equivalent circuit of the proposed system is depicted in Fig. 9.

It can be observed that only one digital-signal-processor (DSP) controller is used to generate all synchronized control signals and only one dc power supply will be needed in the proposed system. Also, the magnetic sensors (TMR 2503) are located at the sensing points to detect the fluctuation of the magnetic field caused by the movement of the receiver coils and thus can derive the feedback of the presence of the users [22].

### B. Circuit Analysis and Current Optimization

Assuming *i*, *k* ($1 \le i, k \le n, i \ne k$) denote the *i*th and *k*th transmitter, the resonant current in the *i*th transmitter coil can be given by

$$\mathbf{I}_i = I_0 \cos(\omega t + \varphi_i) \tag{10}$$

where $\omega$ denotes the system angular frequency and $\varphi_i$ denotes the phase angle displacements whose value is 0 or $\pi$. Consequently, the circuit equations of the system can be expressed as

$$\mathbf{U}_i = j\omega M_{ri}\mathbf{I}_r + j\omega \sum_{k=1}^{n} M_{ik}\mathbf{I}_k + (R_i + jX_i)\mathbf{I}_i \tag{11}$$

$$0 = j\omega \sum_{i=1}^{n} M_{ir}\mathbf{I}_i + (R_{\text{load}} + R_r + jX_r)\mathbf{I}_r \tag{12}$$

where the subscript *r* denotes the receiver. $M_{ik}$ denotes the mutual inductance between *i*th and *k*th coil. $R_i$ and $R_r$ are the parasite resistors of the transmitter and receiver circuit, respectively. $R_{\text{load}}$ is the equivalent resistance of the rectifier

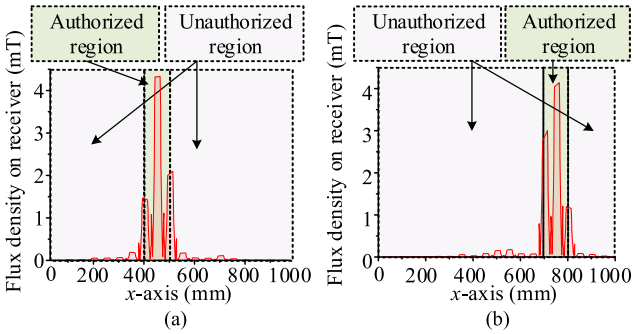


Fig. 10. Magnetic flux density on the receiver. (a) Target on the 5th coil. (b) Target on the 8th coil.

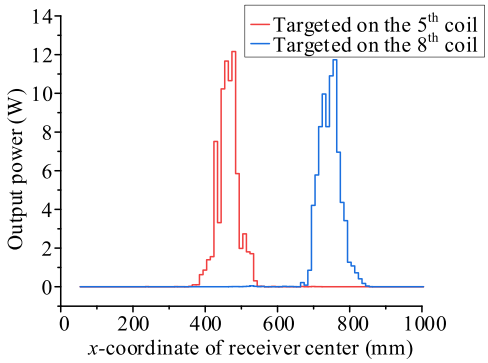


Fig. 11. Output power versus position of receiver.

and the load resistor. $X_i$ is given by

$$X_i = \omega L_i - \frac{1}{\omega C_i}. \tag{13}$$

Under the fully compensated circumstance, $X_i = 0$. The output power can be expressed as

$$P_{\text{load}} = I_r^2 R_{\text{load}} = \frac{\omega^2 \left(\sum_{i=1}^{n} M_{ir} I_i\right)^2 R_{\text{load}}}{\left(R_{\text{load}} + R_r\right)^2}. \tag{14}$$

Thus, the system efficiency can be derived as

$$\begin{aligned}\eta &= \frac{P_{\text{load}}}{P_{input}} = \frac{P_{load}}{P_{load} + P_{loss}} \\ &= \frac{{I_r}^2 R_{load}}{{I_r}^2 (R_{load} + R_r) + \sum_{i=1}^{n} I_i^2 R_i} \\ &= \frac{R_{load}}{(R_{load} + R_r) + \frac{(R_{load} + R_r) \sum_{i=1}^{n} I_i^2 R_i}{\omega^2 \left(\sum_{i=1}^{n} M_{ir} I_i\right)^2}}.\end{aligned} \tag{15}$$

It can be seen from (15) that with the predetermined controlling currents, a larger $n$ can make the system suffer more heat losses and the transmission efficiency will be diminished. Thus, under the condition that the practical requirements can be satisfied, the system should adopt as small a number of transmitter coils as possible to reduce the extra current losses. The further optimization problem can be modeled as

$$\max P_{\text{load}} \tag{16a}$$

$$s.t.\ \mathbf{I}_i \in \mathbf{S} \quad (i \in [1, p]) \tag{16b}$$

where $\mathbf{S}$ denotes the range sets of the transmitter currents which satisfy (9). Under the circumstance of fixed system angular frequency and resistance, it can be seen from (14) and (15) that maximizing the utilization of the power is equivalent to maximizing the summation of every product of the transmitter current and the corresponding mutual inductance within the current range obtained from (9).

To evaluate the performance of the optimized currents for the system shown in Fig. 7, the magnetic flux density along the $z$-axis when the system is operated at 1 MHz is depicted in Fig. 10. The magnetic field is controlled to be targeted on the 5th coil or the 8th coil and the results are shown in Fig. 10(a) and (b), respectively. Each dataset in the figure is plotted based on the simulated magnetic flux density generated on the receiver in independent cases, in which the receiver is placed at different positions on the sensing line. The distance between the receiver and transmitter array is set to be 100 mm. It can be seen that the magnetic flux density in the authorized region is always much higher than that in unauthorized regions. With the misalignment of the receiver, the induced magnetic flux density through the receiving coil is rapidly decreasing. The simulated output power versus the $x$- coordinate of the receiver center under two different editing scenarios are depicted in Fig. 11. For the 100-mm misalignment from the authorized region, the output power drops over 90%, from 12.37 to 0.39 W. And for the misalignment more than 150 mm, there is barely any difference than the situation of 500-mm misalignment, and there would be hardly a resonant effect at all. At the authorized region, the output power can be kept at a very high level while at the unauthorized region, the output power is nearly zero, no matter the position of the receivers. Thus, the power can be delivered to targeted receivers at specific areas while maintaining a relatively high transmission efficiency.

### C. Control Strategy

The control strategy of hybrid modulation is adopted to control the output voltage at a relatively high resolution [14]. The rms value of the driving voltages needed for each Tx coil can be derived from (11), shown as

$$U_{RMS\_i} = \frac{\sqrt{2}}{2} \left| \frac{\omega^2 M_{ri} \sum_{i=1}^{n} M_{ri} \mathbf{I}_i}{R_{load}} + R_r + jX_i + j\omega \sum_{k=1}^{n} M_{ik} \mathbf{I}_k + (R_i + jX_i)\mathbf{I}_i \right|. \tag{17}$$

Each control signal is combined by two components with the frequencies of $f_r/(2n \pm 1)$, respectively, where $f_r$ denotes the system frequency. Assuming

$$\sigma_i = \frac{U_{RMS\_i}}{U_{RMS\_\max}} \tag{18}$$

the duty ratio of the two different components can be obtained from

$$\sigma_{di} = \frac{N_1}{N_1 + N_2} = \frac{(2n+1) - (1/\sigma_i)}{2} \tag{19}$$

where $N_1$ and $N_2$ are two integers denoting the half duty cycle numbers of the two components. The frequency-division factor $n$, which is also an integer, can be chosen based on the range of $\sigma_i$, shown as

$$\frac{1}{(2n+1)} \le \sigma_i \le \frac{1}{(2n-1)}. \tag{20}$$

For the maximum output voltage, $n = 1, N_1 = 1, N_2 = 0$. By applying Fourier analysis, the half-bridge output voltage can be expressed as [23]

$$U(t) = DV_{dc} + \sum_{n=1}^{\infty} \frac{2V_{dc}\sin(n\pi D)}{n\pi} cos(n\omega t) \tag{21}$$

where $V_{\rm dc}$ denotes the input dc voltage and $D$ denotes the duty cycle of each working period, whose value is chosen to be 0.5 here. The rms value of the fundamental component can be given as

$$U_{RMS} = \frac{\sqrt{2}V_{dc}}{2\pi}. \tag{22}$$

Thus, the dc voltage can be determined by (22) and the maximum value of $U_{\rm RMS}$. Based on (17)–(22), the transmitter currents and hence the magnetic flux density can be adjusted by the duty cycle of the two components of the controlling signal. Another key issue in the controlling process is to guarantee the currents to be synchronized to exactly 0 or 180° phase angle. The waveform of the transmitter currents must be exactly the exact or opposite phase angle at every time instant. While it can be seen from (11) that the mutual inductance between the transmitter coils will influence the current phase angle. Thus, an extra phase delay $\varphi_c$ for the correction purpose may be needed for the controlling signal. For the $i$th control signal, the delay angle $\varphi_{ci}$ is exactly the phase angle of the input voltages, as shown in (23)

$$\varphi_{ci} = \arctan \frac{\mathrm{Im}(\mathbf{U}_i)}{\mathrm{Re}(\mathbf{U}_i)}. \tag{23}$$

For the reason that the delay angle could not be negative, the value obtained from (23) should be further transferred to $[0, 2\pi]$ based on periodicity.

The typical control waveforms when two transmitter currents are in phase or opposite phase can be demonstrated in Fig. 12(a) and (b), respectively, where $V_g$ is the gate signal. The green dash line is the reference waveform of $V_g$ before the phase delay. It can be seen from Fig. 12 that with the delay angle $\varphi_c$ added to the input signal, the currents can be kept to be exactly in phase or in opposite phase, which satisfies the control requirement. For each checking cycle, the transmitter current determination procedure can be expressed by the flow chart as shown in Fig. 13, where MFD is the magnetic flux density.

The compromised part lies in the maximum efficiency current optimization procedure, which means that the magnetic flux density generated by the optimized current must not be beyond the threshold value of the determined ones. This may cause the maximum efficiency to not be achievable under some circumstances. As mentioned before, the proposed system involves two optimization procedures in total. One is the transmitter current optimization based on the system configuration and the mutual inductances. The other is to find the rightful input voltage and controlling signals to obtain higher output power. The former one is related to the targeting performance and the latter one aims for better system efficiency. Sometimes there would be a tradeoff between the security level and the usage of the energy because some of the transmitter currents are used to null steering the unauthorized area. But on the other hand, the magnetic flux density at authorized regions can be more centralized and utilized with better performance after the predetermined editing process. The tradeoff also exists in the choice of transmitter current numbers. The more the number of currents means more degree of freedom and higher resolution of the editing, whereas the controlling logic will be complicated. Besides, because the mutual inductance is very sensitive to the position relationship between the coils, the topology of the transmitter array can also be optimized, depending on practical requirements.

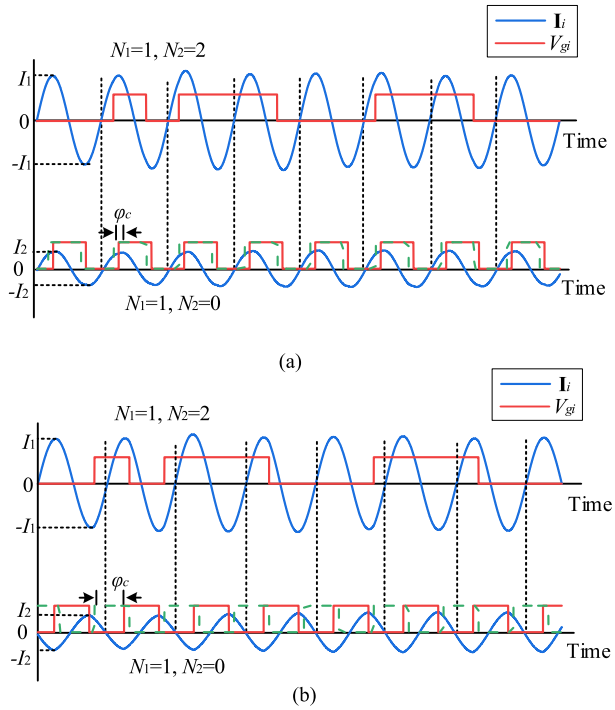


Fig. 12. Typical control waveforms. (a) Two transmitter currents are in phase. (b) Two transmitter currents are in the opposite phase.

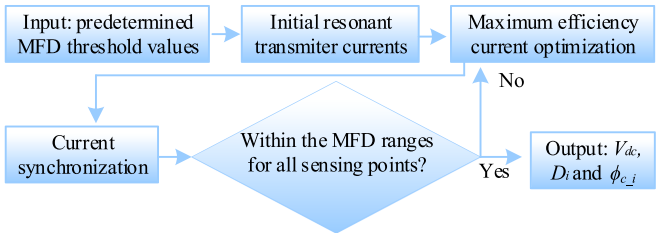


Fig. 13. Flow chart of the control determination procedure.

TABLE III
MEASURED ELECTRICAL PARAMETERS

| Items | Symbol | Value |
|---|---|---|
| Transmitter resistance (averaged) | $R_t$ | 0.58 Ω |
| Transmitter inductance (averaged) | $L_t$ | 38.80 μH |
| Transmitter compensated capacitor | $C_t$ | 652.84 pF |
| Receiver resistance | $R_r$ | 0.60 Ω |
| Receiver inductance | $L_r$ | 36.55 μH |
| Receiver compensated capacitor | $C_r$ | 693.03 pF |
| Load Resistance | $R_{load}$ | 5 Ω |

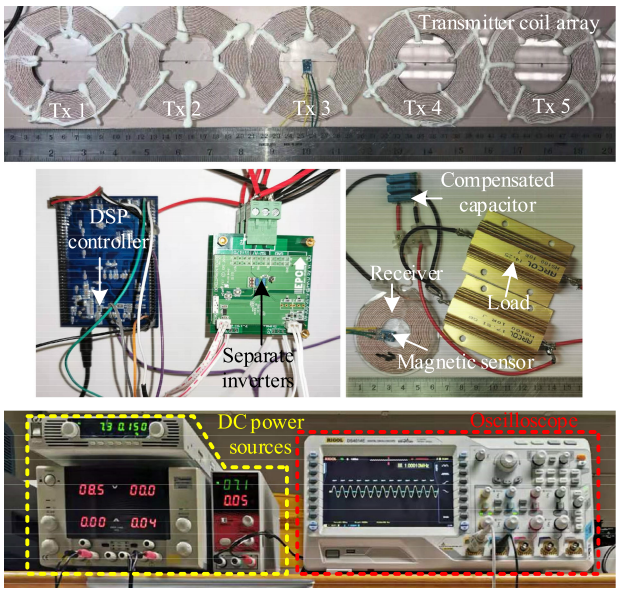


Fig. 14. Experimental setup.

TABLE IV
CURRENT VALUE FOR TWO CASES

| Number | Current for case 1 (A) | Current for case 2 (A) |
|---|---|---|
| 1 | 0.1334 | -0.0062 |
| 2 | -0.4112 | 0.1329 |
| 3 | 1.8010 | -0.4112 |
| 4 | -0.4112 | 1.7906 |
| 5 | 0.1334 | -0.3815 |

## V. EXPERIMENTAL VALIDATION

To further evaluate the performance of the proposed MFE system. Hardware prototype is established and practical experimentation is conducted. The sizes of the transmitter and receiver coils are kept the same with the ones shown in Fig. 7(a). The measured electrical parameters of the system under the frequency of 1 MHz are summarized in Table III. The gallium nitride (GaN)-based inverters are adopted to realize high-frequency resonance. The prototype of the proposed MFE system and the measuring equipment are shown in Fig. 14. Five transmitters are lined up under the sensing line, each is driven by a separate GaN-based half-bridge inverter. The whole system can be driven by a single dc power source. The controlled currents for the five transmitter coils are summarized in Table IV for two different cases, in which the authorized regions are set within the ranges of the 3rd and the 4th transmitter coil, respectively. The distance between the receiver and the transmitter array is set to be 100 mm.

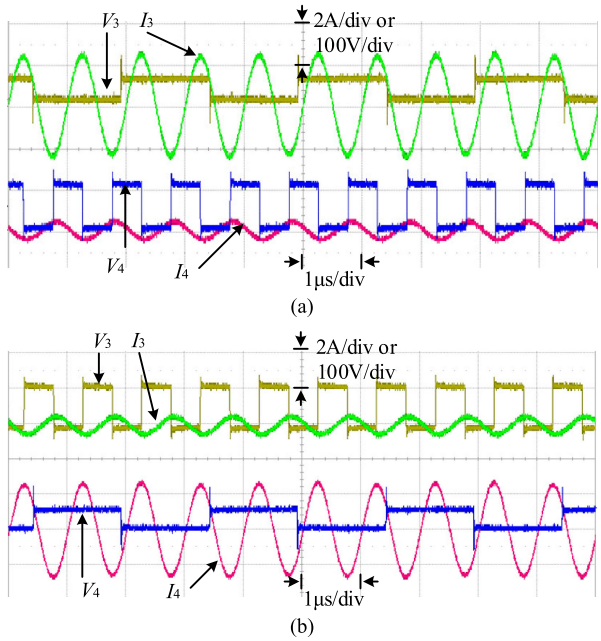


Fig. 15. Measured input waveforms. (a) Case 1. (b) Case 2.

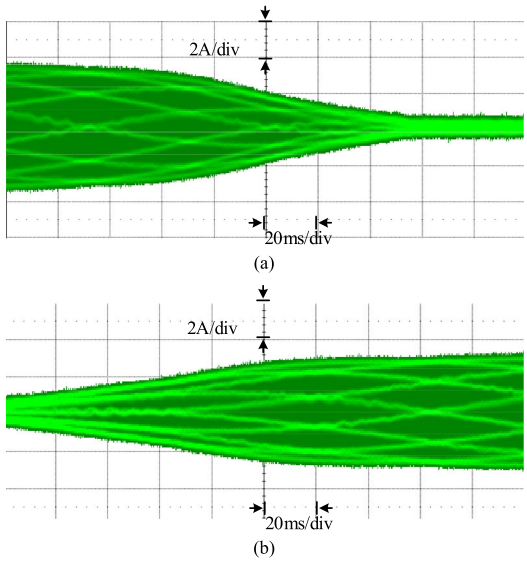


Fig. 16. Dynamic output current. (a) Case 1. (b) Case 2.

The measured input waveforms for the two cases are selectively presented in Fig. 15. It can be seen that with the correcting angle produced by the controller, the transmitter currents can be kept synchronized and the operating frequency is maintained to be 1 MHz. The rms values can also be kept the same as the ones shown in Table IV. The dynamic load current when the receiver is moved from the center of the 3rd Tx coil to the center of the 4th coil for two cases is presented in Fig. 16. It can be seen that the current induced in the receiver in the authorized region will be rapidly decreased from 1.74 A to less than 0.3 A only with a misalignment of 100 mm, and it can also be rapidly raised back when the receiver is moved back to the authorized region. With limitations added to (9), the undesired points can effectively be limited under the threshold output

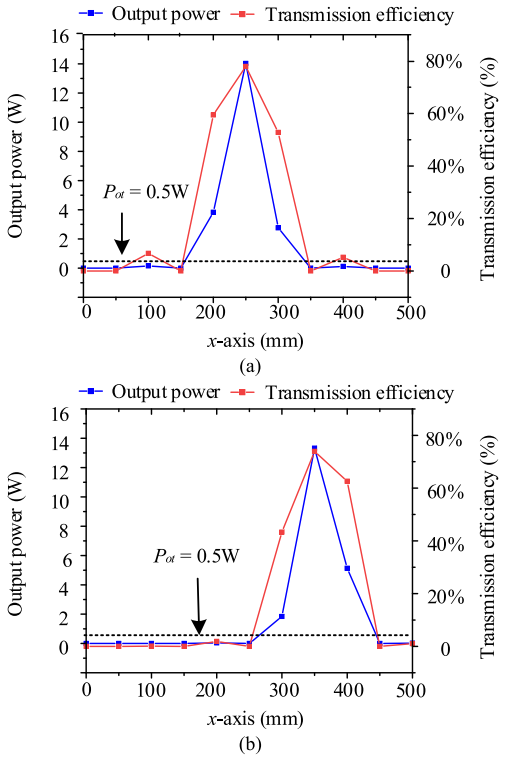


Fig. 17. Measured output power and transmission efficiency under different receiver positions. (a) Case 1. (b) Case 2.

TABLE V
CURRENT VALUE FOR CASE 3

| Number | Current for case 3 (A) |
|---|---|
| 1 | -0.3622 |
| 2 | 1.8041 |
| 3 | -0.7950 |
| 4 | 1.9146 |
| 5 | -0.3872 |

power to keep the electromagnetic emission safe. Therefore, the proposed system can effectively realize the selective WPT based on the receiver's position.

When the receiver is located at different sensing points, the output power and transmission efficiency of the proposed system are measured as depicted in Fig. 17, where $P_{ot}$ denotes the threshold value of the output power. It can be seen that when the receiver is located at the predetermined targeted points, the output power is much higher than the threshold value. The output power can achieve 14 W with the transmission distance three times larger than the radius of the receiver coil. The transmission efficiency of the proposed system can also reach 79.8%.

To further testify the system performance under the multiple-receivers scenario, case 3 is designed and conducted to control the magnetic field to have multiple authorized regions. In this case, two separate authorized regions are set to be within the ranges of 2nd and 4th transmitter coils, respectively. Two identical receivers with the same size, as shown in Fig. 7(a), are adopted. The controlled primary currents are listed in Table V. The results are presented in Fig. 18, where $x_{r1}$ and $x_{r2}$ denote the coordinates of the center of receiver 1 and receiver 2,

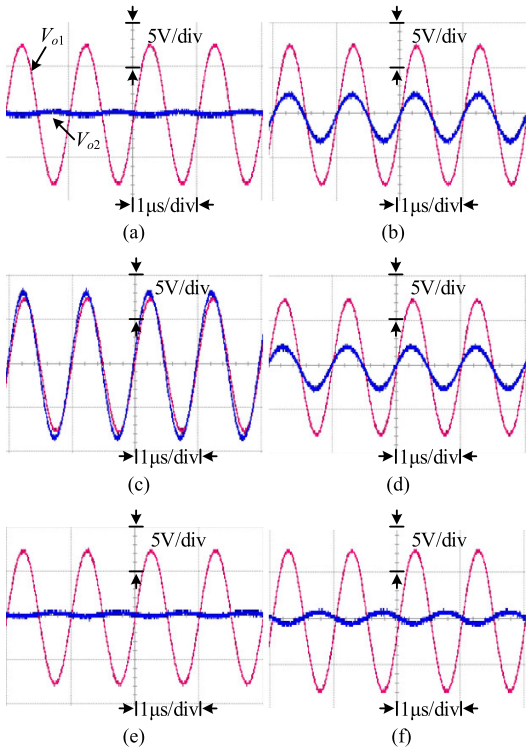


Fig. 18. Typical output waveforms for Case 3. (a) $x_{r1}$ = 150 mm; $x_{r2}$ = 250 mm. (b) $x_{r1}$ = 150 mm; $x_{r2}$ = 300 mm. (c) $x_{r1}$ = 150 mm; $x_{r2}$ = 350 mm. (d) $x_{r1}$ = 150 mm; $x_{r2}$ = 400 mm. (e) $x_{r1}$ = 150 mm; $x_{r2}$ = 450 mm. (f) $x_{r1}$ = 150 mm; $x_{r2}$ = 500 mm.

respectively, and $V_{o1}$ and $V_{o2}$ denote the output voltages of the two receivers.

In the experiment, receiver 1 is kept still in one of the authorized regions while receiver 2 is placed at different positions along the sensing line. Coincided with the theoretical analysis, the output voltage of receiver 1 can be kept at the rated value while for receiver 2, it can have the rated output only when it is within the range of the second authorized region. With 100-mm misalignment, the output voltage of the receiver 2 is rapidly decreased by 89.36% from 7.52 to 0.81 V and barely has any output in these unauthorized regions, which also validates the selectivity of the proposed system.

## VI. CONCLUSION

A new selective WPT system has been proposed and implemented. Based on the proposed MFE technology and control strategy, the system can deliver the power to desired sensing points while inhibiting other sensing points at the same time. Compared to other magnetic beamforming technologies, the transmission efficiency has been significantly improved and can achieve 79.8%. If incorporating more transmitter coils, more sensing positions will be controllable and higher resolution of MFE will be resulted. Another advantage of the system is that the system protocol can be further embedded into various algorithms to adapt to different applications. A prototype of the system is established and tested in practice. The experimental results confirm the viability of the proposed system.

## REFERENCES


[1] Y. P. Fallah, N. Nasiriani, and H. Krishnan, "Stable and fair power control in vehicle safety networks," *IEEE Trans. Veh. Technol.*, vol. 65, no. 3, pp. 1662–1675, Mar. 2016.

[2] R. Jin, X. He, and H. Dai, "On the security-privacy tradeoff in collaborative security: A quantitative information flow game perspective," *IEEE Trans. Inf. Forensics Secur.*, vol. 14, no. 12, pp. 3273–3286, Dec. 2019.

[3] Z. Zhang, K. T. Chau, C. Liu, C. Qiu, and F. Lin, "An efficient wireless power transfer system with security considerations for electric vehicle applications," *J. Appl. Phys.*, vol. 115, no. 17, May 2014, Art. no. 17A328.

[4] S. Aldhaher, D. C. Yates, and P. D. Mitcheson, "Design and development of a class $EF_2$ inverter and rectifier for multi megahertz wireless power transfer systems," *IEEE Trans. Power Electron.*, vol. 31, no. 12, pp. 8138–8150, Dec. 2016.

[5] W. Han, K. T. Chau, C. Jiang, W. Liu, and W. H. Lam, "Design and analysis of wireless direct-drive high intensity discharge lamp," *IEEE J. Emerg. Sel. Topics Power Elect.*, to be published, doi: 10.1109/JESTPE.2019.2948069.

[6] C. Jiang, K. T. Chau, C. Liu, and W. Han, "Design and analysis of wireless switched reluctance motor drives," *IEEE Trans. Ind. Electron.*, vol. 66, no. 1, pp. 245–254, Jan. 2019.

[7] M. Kim, D. Joo, and B. K. Lee, "Design and control of inductive power transfer system for electric vehicles considering wide variation of output voltage and coupling coefficient," *IEEE Trans. Power Electron.*, vol. 34, no. 2, pp. 1197–1208, Feb. 2019.

[8] J. M. Arteaga, S. Aldhaher, G. Kkelis, D. C. Yates, and P. D. Mitcheson, "Multi-MHz IPT systems for variable coupling," *IEEE Trans. Power Electron.*, vol. 33, no. 9, pp. 7744–7758, Sep. 2018.

[9] Z. Zhang and K. T. Chau, "Homogeneous wireless power transfer for move-and-charge," *IEEE Trans. Power Electron.*, vol. 30, no. 11, pp. 6213–6220, Nov. 2015.

[10] G. Yang, M. R. V. Moghadam, and R. Zhang, "Magnetic MIMO signal processing and optimization for wireless power transfer," *IEEE Trans. Signal Process.*, vol. 65, no. 11, pp. 2860–2874, Jun. 2017.

[11] J. Jadidian and D. Katabi, "Magnetic MIMO: How to charge your phone in your pocket," in *Proc. 20th Annu. Int. Conf. Mobile Comput. Netw.*, 2014, pp. 495–506.

[12] B. Clerckx, R. Zhang, R. Schober, D. W. K. Ng, D. I. Kim, and H. V. Poor, "Fundamentals of wireless information and power transfer: From RF energy harvester models to signal and system designs," *IEEE J. Sel. Areas Commun.*, vol. 37, no. 1, pp. 4–33, Jan. 2019.

[13] Z. Zhang, K. T. Chau, C. Qiu, and C. Liu, "Energy encryption for wireless power transfer," *IEEE Trans. Power Electron.*, vol. 30, no. 9, pp. 5237–5246, Sep. 2015.

[14] W. Liu, K. T. Chau, C. H. T. Lee, W. Han, X. Tian, and W. H. Lam, "Full-range soft-switching pulse frequency modulated wireless power transfer," *IEEE Trans. Power Electron.*, vol. 35, no. 6, pp. 6533–6547, Jun. 2020.

[15] B. H. Waters, B. J. Mahoney, V. Ranganathan, and J. R. Smith, "Power delivery and leakage field control using an adaptive phased array wireless power system," *IEEE Trans. Power Electron.*, vol. 30, no. 11, pp. 6298–6309, Nov. 2015.

[16] Y. Lim and J. Park, "A novel phase-control-based energy beamforming techniques in nonradiative wireless power transfer," *IEEE Trans. Power Electron.*, vol. 30, no. 11, pp. 6274–6287, Nov. 2015.

[17] B. H. Choi, J. H. Kim, J. P. Cheon, and C. T. Rim, "Synthesized magnetic field focusing using a current-controlled coil array," *IEEE Magn. Lett.*, vol. 7, 2016, Art. no. 6501504.

[18] M. Kim *et al.*, "High-resolution synthesized magnetic field focusing for RF barcode applications," *IEEE Trans. Ind. Electron.*, vol. 65, no. 1, pp. 597–607, Jan. 2018.

[19] H. Li, J. Fang, S. Chen, K. Wang, and Y. Tang, "Pulse density modulation for maximum efficiency point tracking of wireless power transfer systems," *IEEE Trans. Power Electron.*, vol. 33, no. 6, pp. 5492–5501, Jun. 2018.

[20] H. Sun, F. Zhu, H. Lin, and F. Gao, "Robust magnetic resonant beamforming for secured wireless power transfer," *IEEE Signal Process. Lett.*, vol. 25, no. 8, pp. 1226–1230, Aug. 2018.

[21] E. Alameda-Hernandez, D. Blanco, D. P. Ruiz, and M. C. Carrion, "The averaged, overdetermined, and generalized LMS algorithm," *IEEE Trans. Signal Process.*, vol. 55, no. 12, pp. 5593–5603, Dec. 2007.

[22] W. Han, K. T. Chau, C. Jiang, and W. Liu, "Accurate position detection in wireless power transfer using magnetoresistive sensors for implant applications," *IEEE Trans. Magn.*, vol. 54, no. 11, Nov. 2018, Art. no. 4001205.

[23] Y. Fang, B. M. H. Pong, and R. S. Y. Hui, "An enhanced multiple harmonics analysis method for wireless power transfer systems," *IEEE Trans Power Electron.*, vol. 35, no. 2, pp. 1205–1216, Feb. 2020.


**Xiaoyang Tian** (Student Member, IEEE) received the B.Eng. degree in electrical engineering and automation from Hangzhou Dianzi University, Hangzhou, China, in 2015, and the M.Eng. degree in electrical engineering from North China Electric Power University, Baoding, China, in 2018. He is currently working toward the Ph.D. degree in electrical and electronic engineering with the Department of Electrical and Electronic Engineering, The University of Hong Kong, Hong Kong, China.

His research interests include wireless power transfer techniques, power electronics, and electric vehicle technologies.

**Kwok T. Chau** (Fellow, IEEE) received the B.Sc. (Eng.), M.Phil., and Ph.D. degrees in electrical and electronic engineering from The University of Hong Kong, Pokfulam, Hong Kong, in 1988, 1991, and 1993, respectively.

Since 1995, he has been with The University of Hong Kong, where he is currently a Professor with the Department of Electrical and Electronic Engineering. He has authored nine books and more than 300 journal papers. His research interests include electric and hybrid vehicles, power electronics and drives, and renewable energies.

Prof. Chau is a fellow of the Institution of Engineering and Technology (IET), U.K., and of the Hong Kong Institution of Engineers (HKIE). He is a Chartered Engineer in Hong Kong. He was the recipient of the Changjiang Chair Professorship from the Ministry of Education, China, and the Environmental Excellence in Transportation Award for Education, Training, and Public Awareness from the Society of Automotive Engineers (SAE) International. He currently serves as a Coeditor for the *Journal of Asian Electric Vehicles*.

**Wei Liu** (Student Member, IEEE) received the B.Eng. degree in electrical engineering and automation and the M.Eng. degree in electrical engineering from China University of Petroleum (East China), Qingdao, China, in 2014 and 2017, respectively. He is currently working toward the Ph.D. degree in electrical and electronic engineering with the Department of Electrical and Electronic Engineering, The University of Hong Kong, Hong Kong, China.

He was a Visiting Researcher in the Nanyang Technological University, Singapore, in 2019. His research interests include power electronics, wireless power transfer techniques, and electric vehicle technologies.

**Christopher H. T. Lee** (Senior Member, IEEE) received the B.Eng. (first class hons.) degree and the Ph.D. degree in electrical engineering from Department of Electrical and Electronic Engineering, The University of Hong Kong, Hong Kong, in 2009 and 2016, respectively.

He currently serves as an Assistant Professor in power engineering with the Nanyang Technological University, Singapore, a Visiting Assistant Professor with Massachusetts Institute of Technology, Cambridge, MA, USA, and an Honorary Assistant Professor with The University of Hong Kong. He has authored one book, three book chapters, and about 70 refered papers. His research interests include electric machines and drives, renewable energies, and electric vehicle technologies.